Size Effect on the Surface Finish of Ultra-precision Fly Cutting Multiphase Alloys

Guoqing Zhang[a], Jiaqi Ran[a,*], Suet To[b], Xiaoyu Wu[a], Peng Huang[a], Mikhail P. Kuz'min[c]

[a]Guangdong Provincial Key Laboratory of Micro/Nano Optomechatronics Engineering, College of Mechatronics and Control Engineering, Shenzhen University, Nan-hai Ave 3688, Shenzhen 518060, Guangdong, P.R. China

[b]State Key Laboratory of Ultra-precision Machining Technology, Department of Industrial and Systems Engineering, The Hong Kong Polytechnic University, Kowloon, Hong Kong, P.R. China

[c]Department of Non-Ferrous Metals, Irkutsk National Research Technical University, Irkutsk, Russian Federation

* Corresponding Author / E-mail: ranjiaqi26@szu.edu.cn, Tel: +86-755-26531066, Fax: +86-755-26557471

Abstract: Ultra-precision Fly Cutting (UPFC) is a typical discontinuous cutting process where cutting tool flies simultaneously with the rotation of spindle and cuts the surfaces of workpiece intermittently. To obtain good surface roughness with an acceptable productivity, it is crucial to investigate the influence of cutting chip and tooling movement during the cutting process**.** In UPFC, it is found that the surface rough patterns(SRP), which are affected by sub-millimeter-size cutting chip, are generally formed at the tool-out area of tool feed imprint on the machined surface. The formation of SRP in UPFC is assumed to be affected by size effect, which plays an important role in new surface generation in micro machining process. In this process, tooling cuts through both the surface layer and inner layer grains of workpiece in chip formation process, leading to the formation of surface rough pattern. In this research, the influence of cutting parameters on surface rough pattern is investigated; a hybrid constitutive Johnson Cook model is established and the finite element (FE) simulation by using the established constitutive model is conducted to analyze the generation of SRP. Experimental and simulation results show that when surface grain ratio is larger than 35%, the inconsistent fracture strain between the surface and inner layers is the main reason of fracture formation inside the uncut chip in UPFC process. SRP is thus formed due to the void

formation and tooling movement marks on the machined surfaces. Increasing spindle speed and reducing feed rate minimize the probability of the occurrence of surface rough pattern. Upon addressing the above described eluded issues and with the informative findings, this research thus provides an in-depth understanding of SRP generation affected by size effect in UPFC process and further presents a basis for improving the quality of machined surfaces.

Keywords: Size effect; Ultra-precision Fly Cutting; Surface rough pattern(SRP); Surface layer model; Finite element simulation

1. Introduction

Ultra-precision Fly Cutting (UPFC) is a fly cutting process, in which the single crystal diamond tool flies simultaneously with the rotation of machine tool spindle, and cuts the surfaces of workpiece intermittently [1]. Accompanying with the intermittent rotary cutting, the spindle moves with a raster tool path to cover the whole machining surface. UPFC has been widely used in fabrication of non-rotational symmetric surfaces and complex micro structures such as freeform surfaces, F-theta lens, pyramid and tetrahedron arrays, etc., with the form accuracy down to sub-micron level and surface roughness to nonmetric level [2-3].

Therefore, research on the cutting mechanism of UPFC and its effect on surface finish is an essential topic. In tandem with this, it is crucial to reveal the effect of UPFC mechanism on surface finish in order to improve the quality of machined surfaces. Since the intermittent cutting mechanism of UPFC is quite different from that of other ultra-precision machining processes such as single point diamond turning and micro milling, it may generate different undesirable phenomena which further affect the surface finish of workpiece. To name a few, the intermittent cutting of UPFC causes the plastic deformation of Zn-Al alloy and phase decomposition on the surface layer with the thickness of about 250 nm [4-5]. In addition, heating effect is another tantalizing issue. Wang et al. (2010) explored the cutting-induced heating effect in UPFC process based on the study of the time-temperature-dependent

precipitation of 6061 aluminum alloy and concluded that heating effect induced in UPFC is the main reason for the alignments of precipitates along the cutting direction [6]. The intermittent cutting mechanism of UPFC also leads to the generation of micro waves in the machined surface [7]. Furthermore, UPFC produces impact stress in workpiece during intermittent cutting and whereby causes micro-fracture initiation and smooth wear land at different tool wear stages [8-9]. Tool micro-fracture is imprinted on the machined surface and whereby ridge-shaped pattern is formed, deteriorating the roughness of machined surfaces. Moreover, tool flank wear changes the tool geometry and therefore influences the surface topography and roughness [10-11].

In UPFC, the intermittent cutting mechanism and raster tool path make tool trajectory and tool imprint on the machined surface different from those in other ultra-precision machining processes. Based on the investigation of tool geometry and cutting kinematics, a series of comprehensive research were conducted on the surface generation of UPFC [12-13]. In these researches, geometrical models were established to calculate the data cloud of tool imprints in UPFC and the surface topography could be displayed in 3-dimension plot. The influence of cutting parameters on the surface topography is thus revealed. Furthermore, Cheung et al. (2004) developed a model-based simulation system to predict the cutting performance of UPFC and then optimized the cutting strategies of freeform surfaces [14]. Their further research was done on optimizing the simulation system by considering the cutting mechanics, cutting strategy, and the kinematics of tool-workpiece [15]. Moreover, Cheng et al. (2008) conducted a theoretical and experimental investigation on the nano-surface generation and surface roughness calculation in UPFC from the geometric point of view [16]. Based on their geometric model, the surface roughness of UPFC was thus improved by optimizing cutting conditions and cutting strategy. Furthermore, Kong et al. (2009) conducted a comprehensive research on the factors affecting surface generation in

UPFC and revealed that tool geometry, cutting parameters, cutting strategy, and tool wear are essential factors affecting the super mirror surface generation, while tool path, cutting strategies, and slides motion errors are the key parameters which affect the form accuracy of the machined freeform surfaces [17]. Their further studies were conducted on the establishment of an integrated kinematics error model to analyze the form error of UPFC optical freeform surfaces [18]. On the other hand, workpiece material properties also affect the roughness and form accuracy of the machined surface. Wang et al. (2013) conducted a theoretical and experimental study about the influence of material swelling on surface generation in UPFC and found that the existence of elastic recovery improves the surface finish [19]. Since spindle vibration has multiple effects on the surface generation in UPFC, a series of comprehensive researches about the effect of spindle vibration on the surface generation were performed and the research came out with the following concluding remarks: (i) Coupled-tilting spindle vibration predominantly influences the surface generation of UPFC; (ii) Impulse spindle vibration due to the cutting force pulse leads to the irregular spindle-vibration waves, which causes one of the irregular, lattice-like and stripe patterns or their combination thereof, on the machined surfaces [20-22].

When the dimensions of workpieces are scaled down to a certain value, the physical behaviors and the mechanical response of the workpieces change. This phenomenon is the so-called size effect in material deforming process, typically in material plastic deformation [23]. Deng and Fu have presented a review on the influence of size effect on micro-scaled plastic deformation process, and the portion of surface layer grain is believed to be the reason caused the difference between macro and micro forming [24]. Prasitthipayong et al proposed a research on indentation size effect by applying nanoindentation on an austenitic Fe-Cr-Ni alloy [25]. Chan and Fu investigate the material deformation behavior of the grain size effect in micro extrusion process and influence of size effect on friction is discussed [26]. Bissacco

et al. present a study on the influence of size effect on surface generation during micro milling process and a theoretical model of the generated surface is used and compared with the experimental result [27]. Size effect in material deformation process occurs due to the scaling down of the geometrical size of workpiece and its existence significantly influences the deformation behaviors of micro-scale specimens. Peng et al. established the famous surface layer model by implementing size factor, which represented the influence of size effect, into Armstrong's constitutive model [28]. Later they applied this model into ABAQUS to conduct the simulation of the soft punch stamping process and compare with the actual experimental result [29]. Size effect related material behaviors include the mechanical behavior [30], fracture behavior [31], flow behavior, elastic recovery, fatigue strength [32], surface roughening, and the properties of micro-formed parts [33]. Size effect in indentation is mainly related to indentation size effect, which manifests the increase of hardness when the indentation size is reduced [34]. The size effect in metal cutting, however, is also nontrivial, due to the intensive strain gradient existing in the machining area. According to Kim et al., the 'size effect' characteristics in metal cutting can be observed when the uncut chip thickness has almost the same size of tool edge radius [35]. It is widely assumed that the size effect in metal cutting may be caused by strain rate effect [36]. However, Dinesh et al. did not think that strain rate effect is totally responsible for the size effect in metal cutting, instead, they thought that the intrinsic of size effect in metal cutting is caused by the strain gradient [37]. Size effect has multiple influences on metal cutting process. A direct result of size effect in metal cutting is the unbounded increase of the specific cutting energy with the decrease of uncut chip thickness [38-40]. Other effects include causing burr formation on the machined surface and increase of surface roughness.

The material removing process in UPFC starts from diamond tool cutting into the workpiece surface and ends with the cutting out of workpiece surface. The cutting mechanism

of UPFC makes the chip morphology thinner (zero in theoretical) at its two sides and thicker (tens to hundreds of microns) at its middle. The change of uncut chip thickness along the chip length induces the occurrence possibility of size effect [41]. Actually, size effect in UPFC could be reflected in two aspects: First of all, the ratio of surface layer grains over inner layer grains is bigger; Secondly, at a certain chip length from the tool-in side, the chip thickness is less than the cutting-edge radius. In this research, a theoretical and experimental study on the SRP generation in UPFC was conducted. A series of experiments were done to explore the generation of SRP at tool-out area of tool feed imprints and the influence of cutting parameters on SRP was investigated. In addition, a hybrid constitutive Johnson Cook model was established based on the fracture energy theory and used in finite element simulation of the SRP generation. The research thus provides an in-depth understanding of size effect on the SRP generation in UPFC and lays a basis to avoid or reduce the formation of SRP and eventually to improve the machined surface finish.

2. Experiments

The experiment was conducted on the Precitech Freeform 705G ultra-precision lathe, which has 5-axes including three linear axes and two rotary axes and satisfies the requirement of raster fly cutting. In the experimental setup, workpiece material was mounted on the B-axis routable table through a ‘L’ shaped fixture, a Kistler® dynamometer was installed between the workpiece and fixture, as shown in Fig.1.

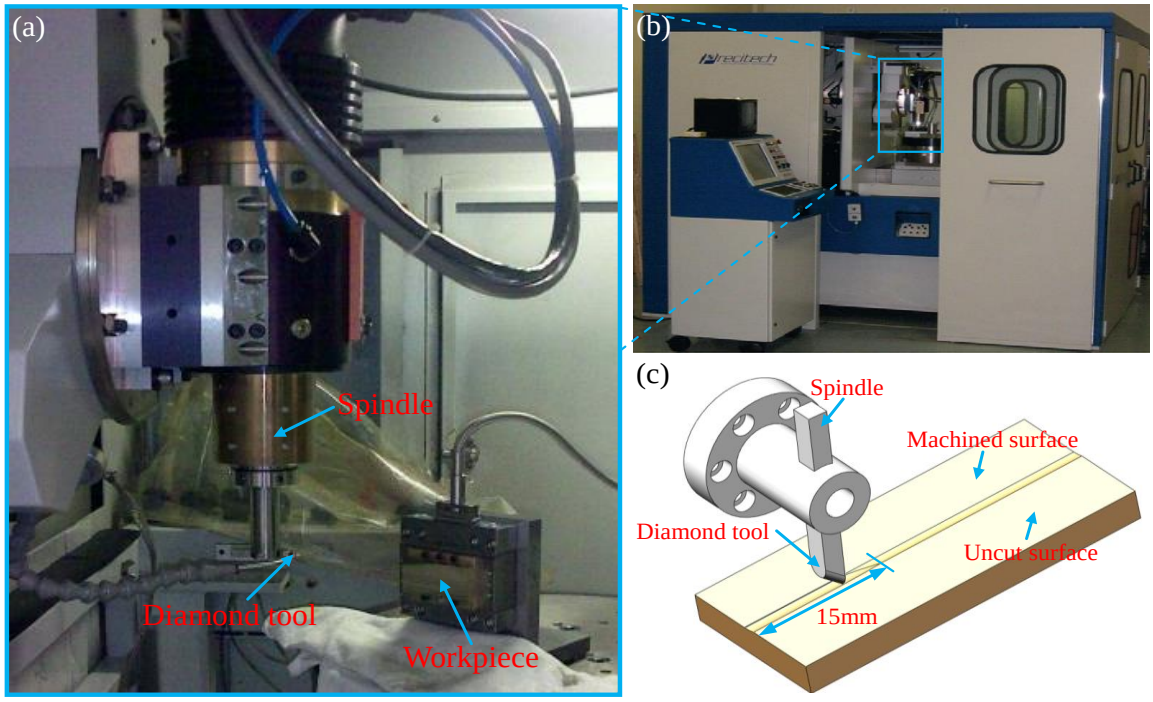

Fig.1 Experimental setup.

In the experiment, a Contour® diamond tool was used to perform the UPFC and brass C3602 was selected as the testing material. To explore the influence of cutting parameters on the formation of SRP, different feed rates, cutting depths and spindle speeds were used in cutting process. For each cutting parameter, 100 raster lines of horizontal cutting were done and a final down-to-up cutting was then conducted at the last raster line. The cutting parameters used in this study are listed in Table 1. During the UPFC process, cutting force was captured through a Kistler 9256C1, the captured force signal was then processed by the Dynoware software. Upon cutting experiment, the machined workpiece was dismounted and measured by an Olympus BX60 optical microscope and a Zygo Nexview white light interferometer respectively.

Table 1.

Cutting parameters used in the experiment

Items	**Cutting**
Tool type	Natural diamond cutting tool

Rake angle	0°
Clearance angle	10°
Tool radius	0.281mm
Feed rate	100, (150), 300, 900mm/min
Step distance	0.02mm
Spindle speed	500, 1500, (3000), 4500rpm
Depth of cut	0.01, (0.02), 0.03, 0.04mm
Swing distance	27.39mm
Cutting strategy	Horizontal cutting

3. Results and discussion

Fig.2 shows the surface image at the spindle speed of 500rpm. It is found that a clear feed boundary occurs on the machined surface, which divides the tool imprints into two parts. In addition, it is found that the surface quality on the different sides of the feed boundary is quite different. It is poor on the upper side of the feed boundary, while smooth on the lower side. The feed boundary is believed to be formed by the intersection of tool imprints in two neighbor rotary cutting circles. However, it is hard to distinguish which side is the tool-in side or tool-out side.

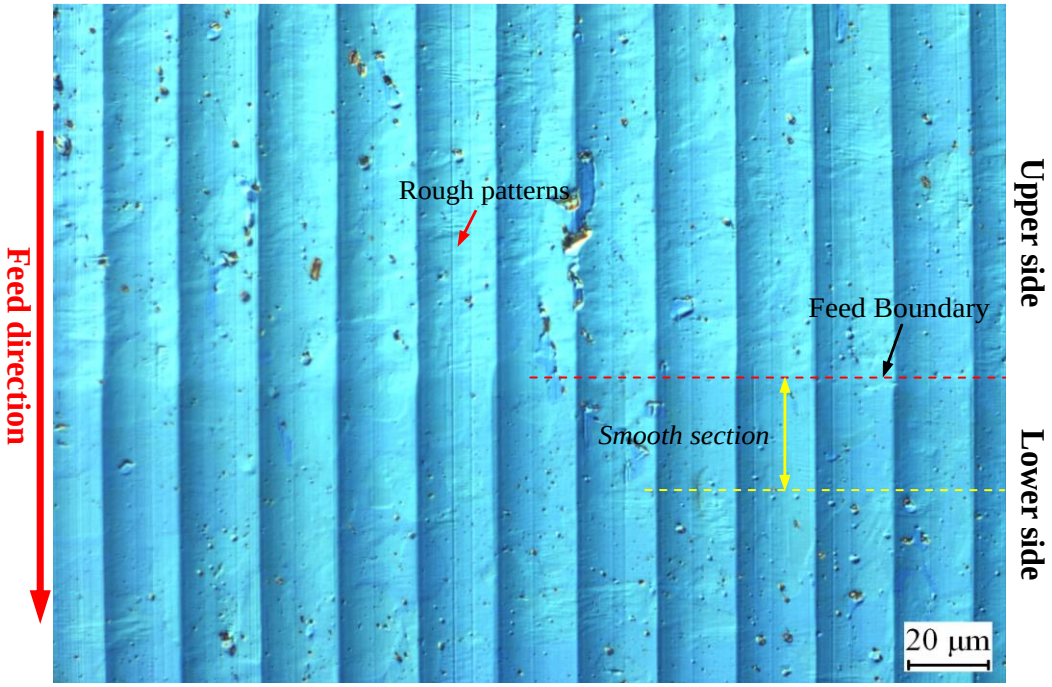

Fig.2 Surface image at the spindle speed of 500rpm

To determine the existence of SRPs on which side of the feed boundary, a final bottom-up cutting was performed. The bottom-up cutting cuts from the machined surface to the uncut surface and presents a whole rotary fly cutting, as shown in Fig. 3. Since the final cutting is a bottom-up cutting, cutting tool is elevated during the final cutting, and thus it is obvious that the SRP exists on the tool-out area of tool feed imprints, as shown in Fig.3(a). Furthermore, it is found from Fig.3 (b) that a smooth section existed on the tool-out closed to the uncut surface, where there is a little rough pattern.

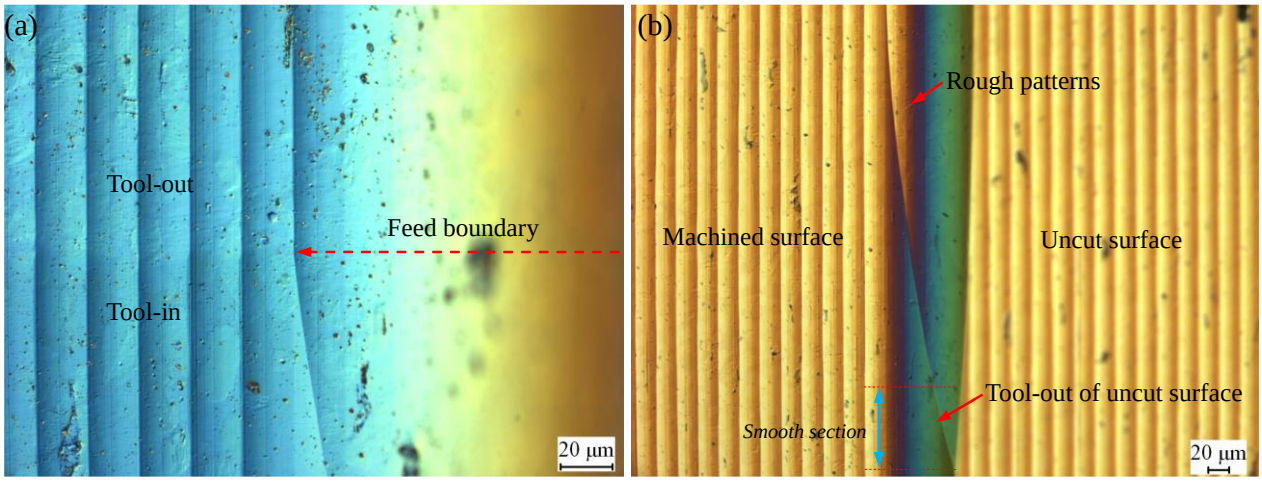

Fig.3 Feed boundary identification in a final bottom-up cutting at the last raster line

The SRPs can also be reflected in the white light interferometer measurement, as shown in Fig.4. It is found that the tool-in area of the measured tool feed imprints is quite smooth, while the tool-out area, however, is quite rough. It is consistent with the results obtained from the optical microscope measurement. Both of them are caused by the formed SRP.

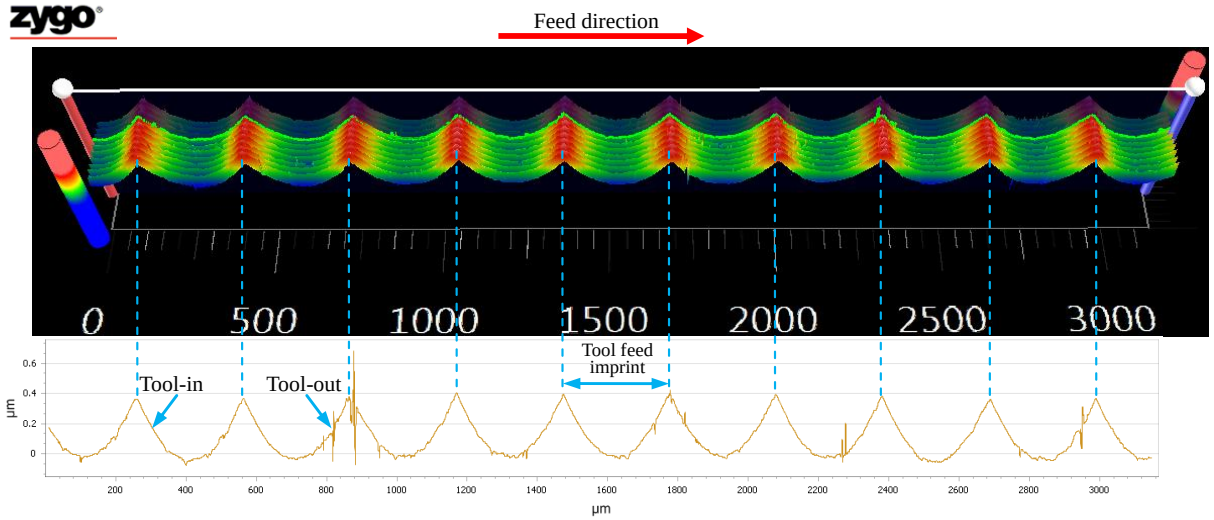

Fig.4 3D topography and the sectional profile of tool feed imprints in a white light interferometer measurement (Zygo Nexview)

The formation of SRP certainly affects the surface finish and even the function of the fabricated products. Since SRP has irregular shape and exists only at the tool-out area of tool feed imprints, it is believed to be caused by the combined effect of the cutting mechanism of UPFC and the material properties of the workpiece.

In UPFC process, the diamond cutting tool flies with the rotation of spindle and cuts the machined surface intermittently. In this process, the discontinuous cutting mechanism makes the diamond tool exert a compressive stress to the workpiece material during cutting into the machined surface, but a tensile stress to the workpiece material during cutting out the machined surface, as shown in Fig.5(a). Therefore, an alternating stress is applied to the workpiece material during the rotary fly cutting, which is quite different from the continuous cutting, e.g. single point diamond turning. In addition, due to the small cutting depth with respect to the swing distance (radius of the spindle rotation trajectory), the contact between

cutting tool and workpiece during the cutting is quite short, as is shown in Fig.5 (b). The short contact can also be reflected from the captured cutting force, as shown in Fig.5(c) which indicates that the cutting duration only takes up about 1% of the whole fly cutting cycle, while the cutting conducts an air cutting in most of the fly cutting cycle.

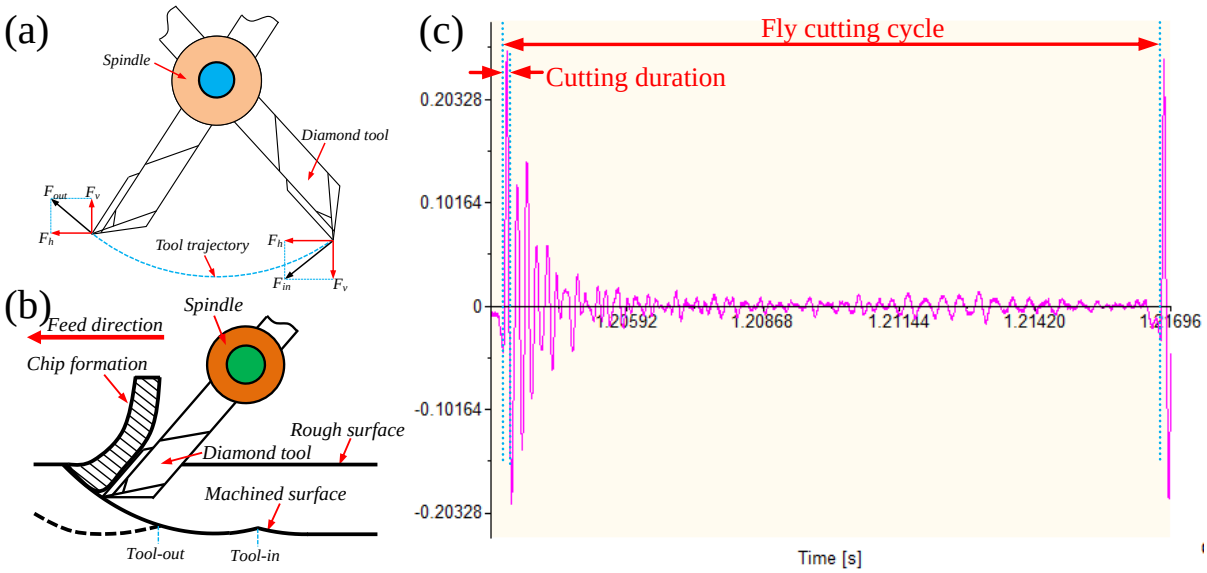

Fig.5 Schematic of fly cutting process and the corresponding cutting force

In UPFC, each rotary cutting produces fresh slope surface. The surface layer grains on the fresh slope surface have more free surfaces and without constraint. Their mechanical property is very similar to that of monocrystalline. The inner layer grains, however, do not have free surface and their mechanical property is like the polycrystalline. Since the uncut chip thickness in UPFC varies from zero to tens of microns and then drops to zero again, and the size of surface layer grain falls into the size scale of ten microns. The rotary fly cutting during chip generation inevitably cuts through both of the surface layer and inner layer grains. According to the cutting chip morphology and the surface layer grain thickness, the surface layer grains take up more than 35% of the total grains and the surface layer grain property cannot be neglected. Therefore, the formation of SRP in UPFC process is generally believed to be caused by the size effect.

4. Finite element simulation

In many prior arts, size effect has been studied and the so-called surface layer model was implemented into Armstrong's model to represent the influence of size effect. In this research, how the geometrical size effect and the phase properties of multiphase alloys affect the machined surface was studied. First of all, size factor was introduced to the widely-used Johnson Cook model in such a way to represent the influence of size effect and A hybrid constitutive model was thus then established. Secondly, finite element simulation by using the developed hybrid constitutive model was conducted. The comparison between simulation and experimental results was finally done and the validation of the hybrid constitutive model was also conducted.

4.1 Johnson Cook model and surface layer model

The general expression of Johnson Cook model is a product of three terms, which represent the influence of material property, strain rate $\dot{\varepsilon}$ and deformation temperature T_w on flow stress σ, as designated in the following Eq.(1) [42].

$$\sigma = [A + B\varepsilon^n][1 + CIn\frac{\dot{\varepsilon}}{\dot{\varepsilon}_0}][1 - \left(\frac{T_w - T_r}{T_m - T_r}\right)^m] \quad (1)$$

The formulation of the first term in Eq.(1) is usually characterized as $A + B\varepsilon^n$ by using Schmid method, which makes the curve fitting easier for considering only two unknown coefficients *A*, *B* and hardening coefficient *n*. The second term in the equation introduces the unknown coefficient *C* to describe the strain rate effect by using the data of Split Hopkinson Pressure Bar experiment (SHPB) for curve fitting. For the third term, the influence of working temperature T_w is considered. Compared with other constitutive models such as Armstrong model, Johnson Cook model has only five unknown coefficients, which can be obtained with upsetting experiment and SHPB experiment and can solve various mechanical problems under different strain rates.

In this research, to explore the phenomenon that tool-in area of a tool feed imprint has a smooth surface while tool-out area has some SRPs, the surface layer model, which considers the workpiece consisting of two layers, viz., surface and inner layers, was thus implemented into the Johnson Cook model. The surface layer grains are easier to deform in plastic deformation as part of these grains have free surfaces without constraint on deformation. The basic formulation of surface layer model is denoted as:

$$\sigma = \frac{N_s\sigma_s + N_i\sigma_i}{N} = \eta\sigma_s + (1-\eta)\sigma_i, (N = N_s + N_i, \eta = \frac{N_s}{N}) \quad (2)$$

where $\sigma, \sigma_s, \sigma_i$ represent the total flow stress, the flow stress of surface grains, and the flow stress of inner grains, respectively. N, N_s, N_i denote the total grain number, surface grain number and inner grain number, η is defined as the size factor. When the compression g experiment by using the normal size specimens is conducted, the influence of surface layer grains is very small as the surface grain number is usually less than 2% of the total grain number. In micro-scale cutting, however, the influence of size effect cannot be ignored as the ratio of surface grains is increased to the range of 35% to 55%, depending on the area affected by cutting force. The red area shown in Fig.6 is the surface layer grains. Fig.6 also indicates that the deformation in cutting process is partially similar to compression process, in which part of the specimen is under compression and thus shear stress is increased. Stress is raised up to yield stress, leading to plastic deformation and slip along 45-degree line to which direction until the plastic strain reaches the fracture strain. The chip is thus removed from workpiece.

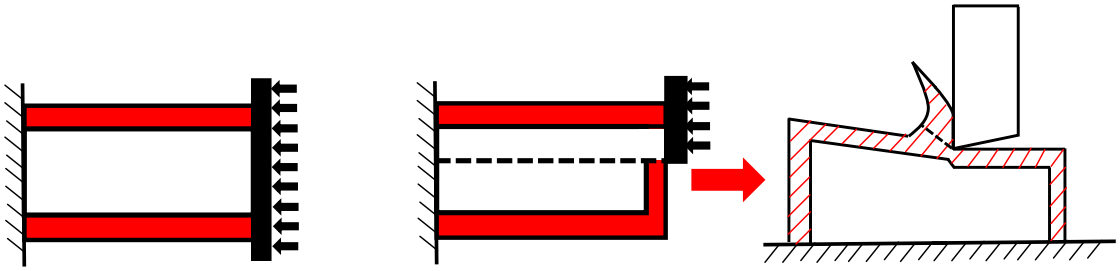

Surface grain ratio: <2%
(2x3mm cylinder billet)

Surface grain ratio: >35%
(Area affected by cutting force)

(a) Upsetting process (b) Partial compression process (c) Cutting process

Fig.6 Surface grain ratio in different deformation processes

Prior arts in this area provide an in-depth understanding of size effect and surface layer model [43]. According to Hall-Petch Equation [44], Hansen's research [45], crystal plasticity theory [46], and Armstrong's research [47, 48], shear stress $\tau(\varepsilon)$ can be represented by lattice friction stress $\tau_0(\varepsilon)$ and the interaction among dislocations. For a given specific strain, $\tau_0(\varepsilon)$ and $k(\varepsilon)d^{-\frac{1}{2}}$ are constant and thus designated as the Hall-Petch equation in the following Eq. (3) [43].

$$\left.\begin{aligned} &\sigma = M\tau \\ &\sigma = \sigma_0 + kd^{-\frac{1}{2}} \\ &\tau(\varepsilon) = \tau_0(\varepsilon) + k(\varepsilon)d^{-\frac{1}{2}} = \tau_0(\varepsilon) + \alpha\mu b\sqrt{\rho_T} \end{aligned}\right\} \Rightarrow \sigma(\varepsilon) = M\tau(\varepsilon) = M\left(\tau_0(\varepsilon) + \alpha\mu b\sqrt{\rho_T}\right) \quad (3)$$

In Eq. (3), *d* is the grain size of testing specimen; *M* is Taylor factor. τ is micro-scaled shear stress. α is a particular constant to describe the dislocation interaction for the multiphase alloys. μ is the corresponding shear module for different phases, *b* is the Burgers vector for FCC and BCC phases. ρ_T is the total dislocation density. The stress contributions of the surface layer and inner layer grains are thus expressed in the following equation [43]:

$$
\begin{cases}
\sigma = \sigma_s(\varepsilon) + \sigma_i(\varepsilon) \\
\sigma_s(\varepsilon) = m\tau_0(\varepsilon) = mk_1\varepsilon^{n_1} \\
\sigma_i(\varepsilon) = \sum \sigma_i f_i \\
\qquad = \sigma_\alpha f_\alpha + \sigma_\beta f_\beta \\
\qquad = \left(Mk_2\varepsilon^{n_2} + \alpha M \mu_\alpha b_\alpha \sqrt{\rho_{T\alpha}(\varepsilon)}\right) f_\alpha + \left(Mk_2\varepsilon^{n_2} + \alpha M \mu_\beta b_\beta \sqrt{\rho_{T\beta}(\varepsilon)}\right)(1 - f_\alpha) \\
\qquad = \left(Mk_2\varepsilon^{n_2} + \alpha M \mu_\alpha b_\alpha \sqrt{\dfrac{C_1\varepsilon}{b_\alpha d}}\right) f_\alpha + \left(Mk_2\varepsilon^{n_2} + \alpha M \mu_\beta b_\beta \sqrt{\dfrac{C_2\varepsilon}{b_\beta d}}\right)(1 - f_\alpha)
\end{cases}
\tag{4}
$$

where m is the grain orientation factor of the surface layer grains; $\sigma_s(\varepsilon)$ and $\sigma_i(\varepsilon)$ are the stress contribution of surface layer grains and inner layer grains; $\sigma_\alpha, \sigma_\beta, f_\alpha$ and f_β are the stress and volume fraction of α phase and β phase of multiphase alloy. n_1, n_2 are hardening coefficients; k_1, k_2, C_1 and C_2 are material constants. The second equation in Eq. (4) represents that the mechanical property of surface layer grains is similar to that of single crystal according to Armstrong's research [42]. For inner layer grains, the polycrystal model designated in Eq. (3) was used.

In this research, Eq. (4) can be further developed as:

$$
\begin{cases}
\sigma_{cuttingarea}(\varepsilon) = \sigma_{se}(\varepsilon) + \sigma_{ie}(\varepsilon) \\
\sigma_{se}(\varepsilon) = \dfrac{\sigma_s(\varepsilon)}{N_s} \bullet N_{se} = \dfrac{mk_1\varepsilon^{n_1}}{N_s} \bullet N_{se} \\
\sigma_{ie}(\varepsilon) = \dfrac{\sigma_\alpha(\varepsilon)}{N_\alpha} \bullet N_{\alpha e} + \dfrac{\sigma_\beta(\varepsilon)}{N_\beta} \bullet N_{\beta e} \\
\sigma_\alpha(\varepsilon) = \left(Mk_2\varepsilon^{n_2} + \alpha M \mu_\alpha b_\alpha \sqrt{\dfrac{C_1\varepsilon}{b_\alpha d}}\right) f_\alpha \\
\sigma_\beta(\varepsilon) = \left(Mk_2\varepsilon^{n_2} + \alpha M \mu_\beta b_\beta \sqrt{\dfrac{C_2\varepsilon}{b_\beta d}}\right)(1 - f_\alpha)
\end{cases}
\tag{5}
$$

where $\dfrac{\sigma_s(\varepsilon)}{N_s}, \dfrac{\sigma_i(\varepsilon)}{N_i}$ denote the stresses of the single grains in the surface layer and inner

layer; $N_{se}, N_{\alpha e}, N_{\beta e}$ represents the number of surface layer grains, α phase grains, and β phase grains existing in the area of workpiece but affected by the cutting force, including the chip removed from the workpiece. The first term of Johnson Cook model cannot explain the reason why the SRP is formed on the tool-out area. Although Eq. (5) has many unknown variables which make curve fitting much more difficult, it is believed that the increasing ratio of surface grains is the main reason for the sudden change of surface roughness. Therefore, Eq. (5) is implemented to replace the first set of the original Johnson Cook model.

The coefficient C in Johnson Cook model is usually obtained by SHPB experiment to describe the influence of strain rate to true stress-strain curve. After comparing the SHPB data and static upsetting data of 2mm and 1mm diameter, it is difficult to use Johnson Cook model to conduct curve fitting because stress increasement of micro-scaled billet is much higher than macro-scaled billet. The strain rate size effect coefficient D is thus implemented to Johnson Cook model to describe the size effect influence to stress strain curve under high strain rate.

The Hybrid Constitutive Johnson Cook (HCJC) model is thus formulated in the following:

$$\sigma=\left[\begin{array}{l}\dfrac{N_{se}}{N_s}\bullet mk_1\varepsilon^{n_1}+\dfrac{N_{\alpha e}}{N_\alpha}\bullet\left(Mk_2\varepsilon^{n_2}+\alpha M\mu_\alpha b_\alpha\sqrt{\dfrac{C_1\varepsilon}{b_\alpha d}}\right)f_\alpha \\ +\dfrac{N_{\beta e}}{N_\beta}\bullet\left(Mk_2\varepsilon^{n_2}+\alpha M\mu_\beta b_\beta\sqrt{\dfrac{C_2\varepsilon}{b_\beta d}}\right)(1-f_\alpha)\end{array}\right][1+C^*In\frac{\dot{\varepsilon}}{\dot{\varepsilon}_0}][1+\eta D][1-\left(\frac{T_w-T_r}{T_m-T_r}\right)^m] \quad (6)$$

To implement the above described research, a general methodology is proposed and illustrated in Fig.7. From the figure, it is clear that for one effective strain, three effective stresses can be obtained with three different grain sizes. The function between grain size and effective stress can be established when a series of effective strains are applied. $\tau(\varepsilon)$ and $\dfrac{k(\varepsilon)}{\sqrt{d}}$ in Eq.(3) is thus calculated. After using curve fitting to determine the unknown

coefficients in Eq.(6), the final formation of HCJC model is thus carried out.

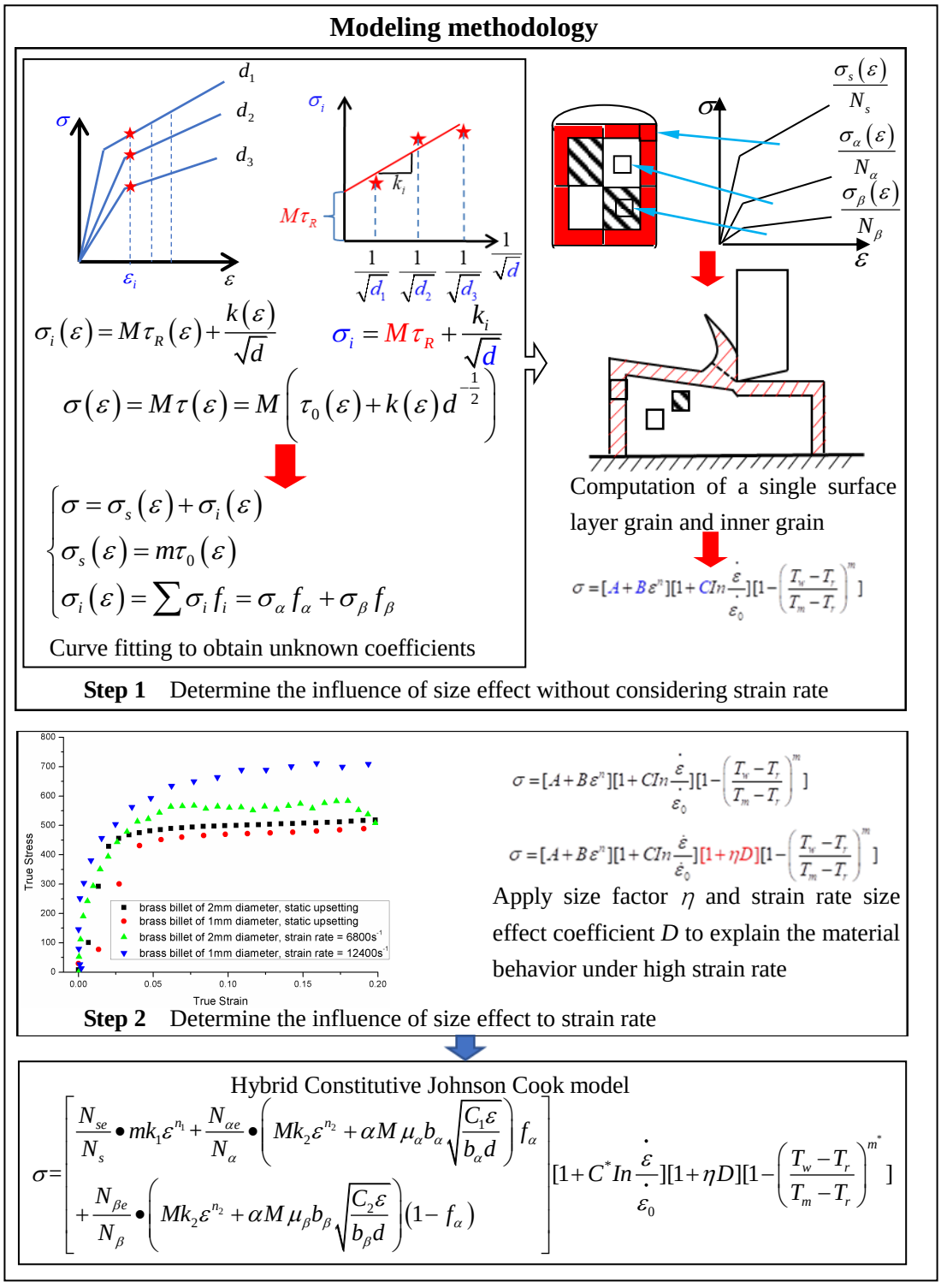

Fig.7 Modeling methodology of HCJC model

4.2 Calculation of the influence of size effect on strain rate in HCJC model

In Eq. (6), d = 18.54μm; m = 2; M=3.06; $\alpha=0.34$ [49]; μ_α=78500 MPa (Shear

modulus for FCC phase); μ_β=72000 MPa (Shear modulus for BCC phase); $b_\alpha = \frac{\sqrt{2}}{2} \times 3.69 \times 10^{-10} = 2.608 \times 10^{-10}$ m (Burgers vector for FCC phase); $b_\beta = \frac{\sqrt{3}}{2} \times 2.94 \times 10^{-10} = 2.546 \times 10^{-10}$ m (Burgers vector for FCC phase). By applying EDX result and examined with sharpened the metallurgical photo, the volume fraction of α, β and Lead phase is obtained as 81%, 17% and 2%. By conducting SHPB experiment, it is found that the true stress strain curve of micro scale (1mm diameter) is much higher than macro scale. The yield stress of high strain rate in macro scale has only increased 15.6% while the yield stress of high strain rate has increased 57.6%, as shown in Fig.8. It is obvious that strain rate size effect coefficient is required when using Johnson Cook model to explain the true stress-strain curve in both low and high strain rate.

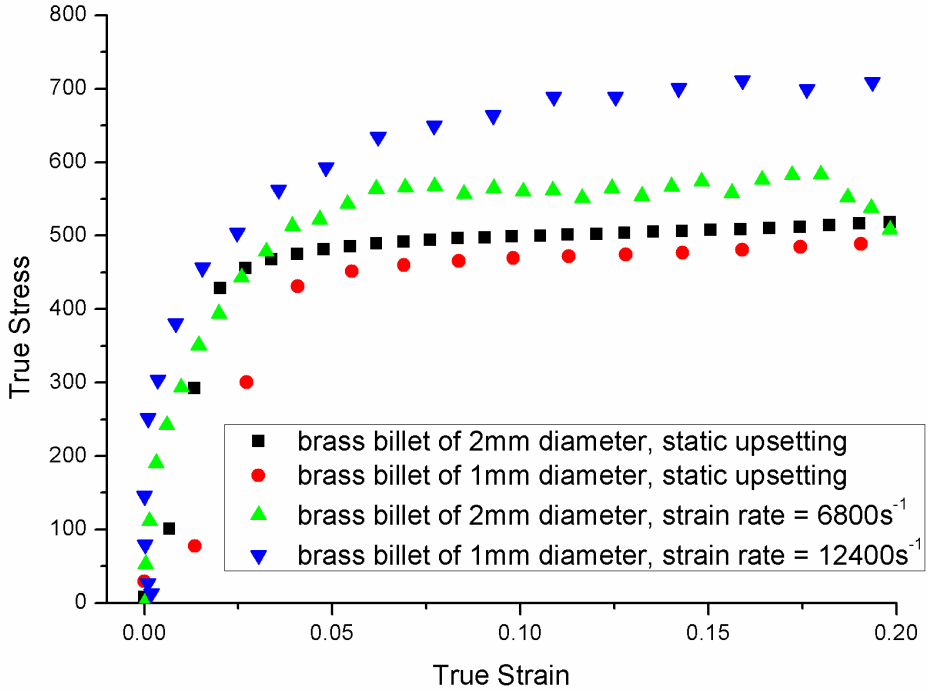

Fig.8 True stress-strain curve of brass C3602 under low and high strain rate

Under the condition of static forming, strain rate will be very low and approximate to zero. T_w is the room temperature. Therefore, Eq. (6) is simplified as:

$$\sigma=\left[\begin{array}{l}\dfrac{N_{se}}{N_s}\bullet mk_1\varepsilon^{n_1}+\dfrac{N_{\alpha e}}{N_\alpha}\bullet\left(Mk_2\varepsilon^{n_2}+\alpha M\mu_\alpha b_\alpha\sqrt{\dfrac{C_1\varepsilon}{b_\alpha d}}\right)f_\alpha \\ +\dfrac{N_{\beta e}}{N_\beta}\bullet\left(Mk_2\varepsilon^{n_2}+\alpha M\mu_\beta b_\beta\sqrt{\dfrac{C_2\varepsilon}{b_\beta d}}\right)(1-f_\alpha)\end{array}\right][1+C^*][1+\eta D] \tag{7}$$

In Eq. (7), the unknown coefficients are k_1, k_2, n_1, n_2, C_1, C_2, C^* and $k_1 = k_2$, $n_1 = n_2$. By applying upsetting experiment data of 2x3mm, 1x1.5mm and 0.5x0.75mm with the grain size of 18.54, 24.21, 45.48, 87.73μm and curve fitting, $k_1 = k_2 = 184.6$, $n_1 = n_2 = 0.17$, $C_1 = 0.11$, $C_2 = 0.17$. Fig.9 has shown the curve fitting process for k, n and C. According to Eq. (3), for a specific strain, such as ε=0.1, four stresses can be obtained with four grain sizes. For a series of strain, a series of $\tau(\varepsilon)$ and $\dfrac{k(\varepsilon)}{\sqrt{d}}$ can be determined and thus determined the value of k, n and C. By applying the data of SHPB, $C^*=0.16$, $D=46.04$, $m^*=1.09$. The final expression for HCJC is designated as:

$$\sigma=[559.58\varepsilon^{0.17}+101.75\varepsilon^{0.5}][1+0.16In\frac{\dot{\varepsilon}}{\dot{\varepsilon}_0}][1+46.04\eta][1-\left(\frac{T_w-T_r}{T_m-T_r}\right)^{1.09}] \tag{8}$$

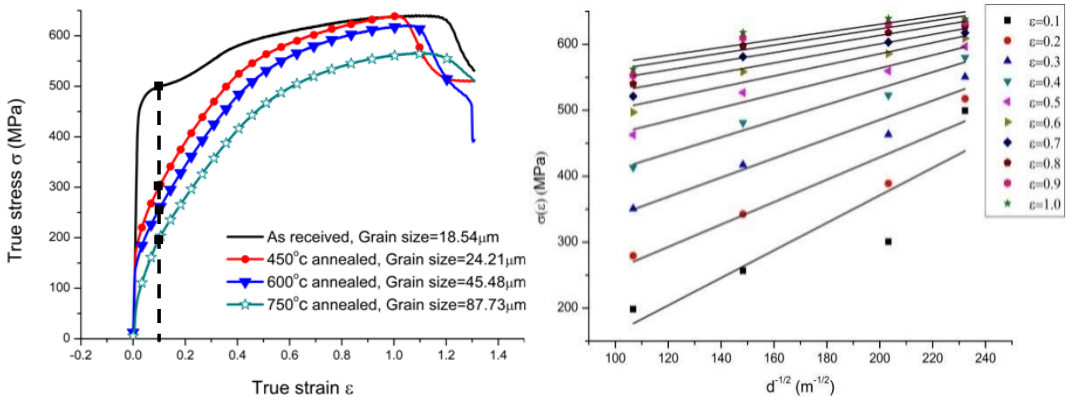

Fig.9 Determination of the unknown coefficients for HCJC model

Comparing the stress-strain curve obtained via Eq. (8) with actual experiment result, it is found that HCJC model coincides with the experiment, which indicates that HCJC model is effective, as shown in Fig. 10.

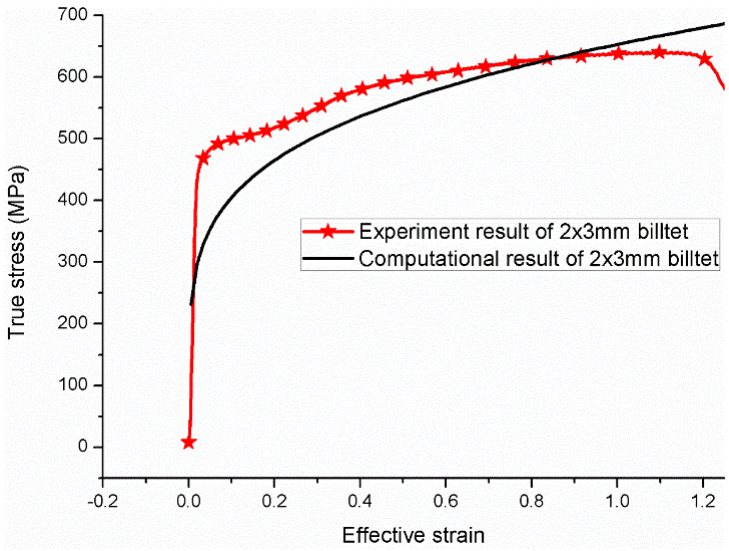

Fig.10 Experimental and computational result of HCJC model on upsetting of 2x3mm billet

The effective stress strain relationship of a single surface layer and inner layer grain is demonstrated in Fig.11 (a). It is obvious that the strain energy a single surface layer grain is about 10 times larger than the inner layer grain. In UPFC process, the surface layer grain number is over 35% of the total grain number, and the strain energy contribution of surface grain layer and inner grain layer is shown in Fig.11. It is clear that the strain energy of surface layer is about 6 times of inner grain layer.

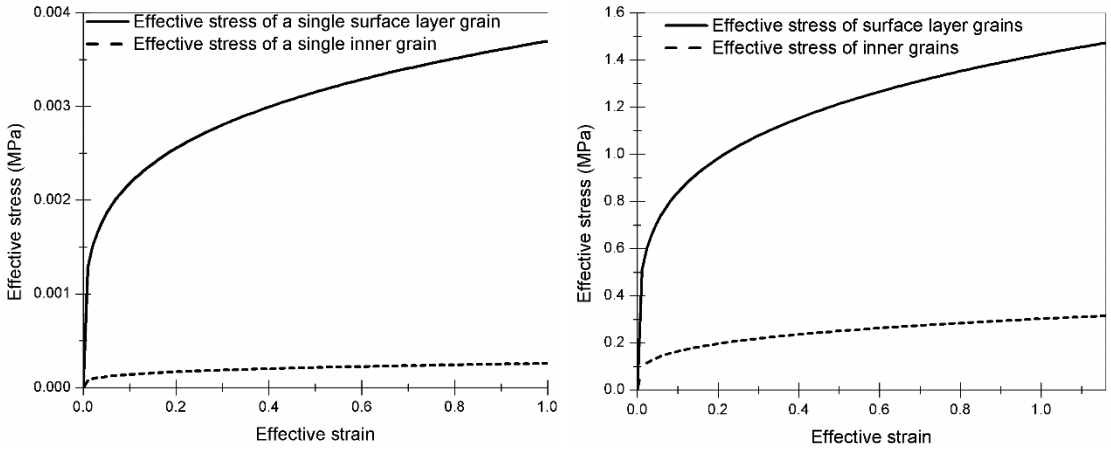

(a) Effective stress of single grain (b) Effective stress of grain layer

Fig.11 Single grain and grain layer strain energy comparison

5. SRP formation and suppression

Based on the derived HCJC model, a two-dimension finite element (FE) simulation of

the UPFC process was conducted in the Abaqus® FEA software. To simulate the rotary fly cutting process, this research transforms the rotary fly cutting in UPFC into an orthogonal cutting according to the chip geometry. Therefore, the chip generation process in UPFC can be successfully simulated in a orthogonal straight cutting simulation, as is shown in Fig.12.

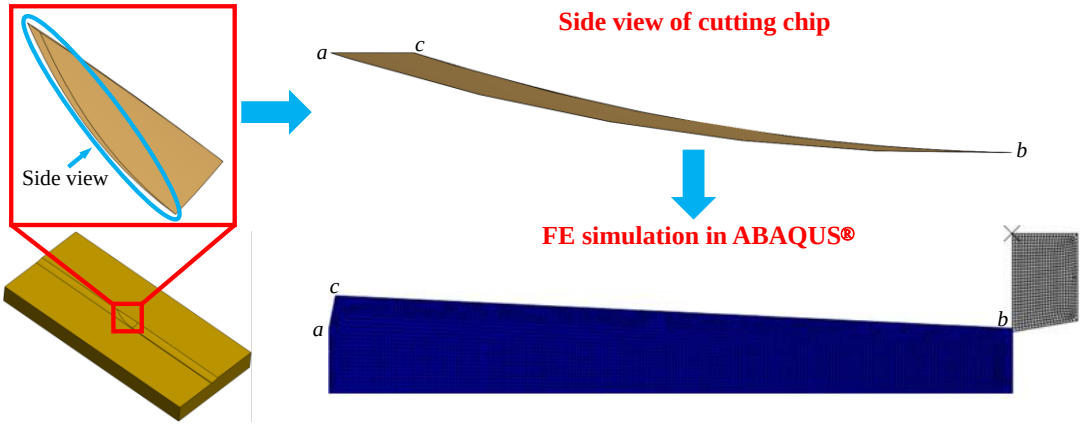

Fig.12 Cutting kinematics transforms in Abaqus® FE simulation

Fig.13 demonstrates the FE simulation result of chip formation in UPFC. In the tool-in area, cutting chip initially forms, the surface layer is cut with shear force performed by cutting tool and damaged under shear stress. In the middle of the chip formation, the inner layer around the corresponding surface layer has formed voids before cutting tool arrives, following tool cut these voids and forms marks, as is shown Fig.13. According to the authors' previous research [43] and Hillerborg's research [50], the reason of damage initiation and crack formation in shear deformation is that the energy absorbed from outside has exceeded the strain energy of the workpiece during cutting process. As the surface strain energy is much higher than inner grain strain energy, the inner grains will reach fracture strain long before surface grains. This means that the inner grains of the chip will be completely damaged and formed major cracks before tooling reach them.

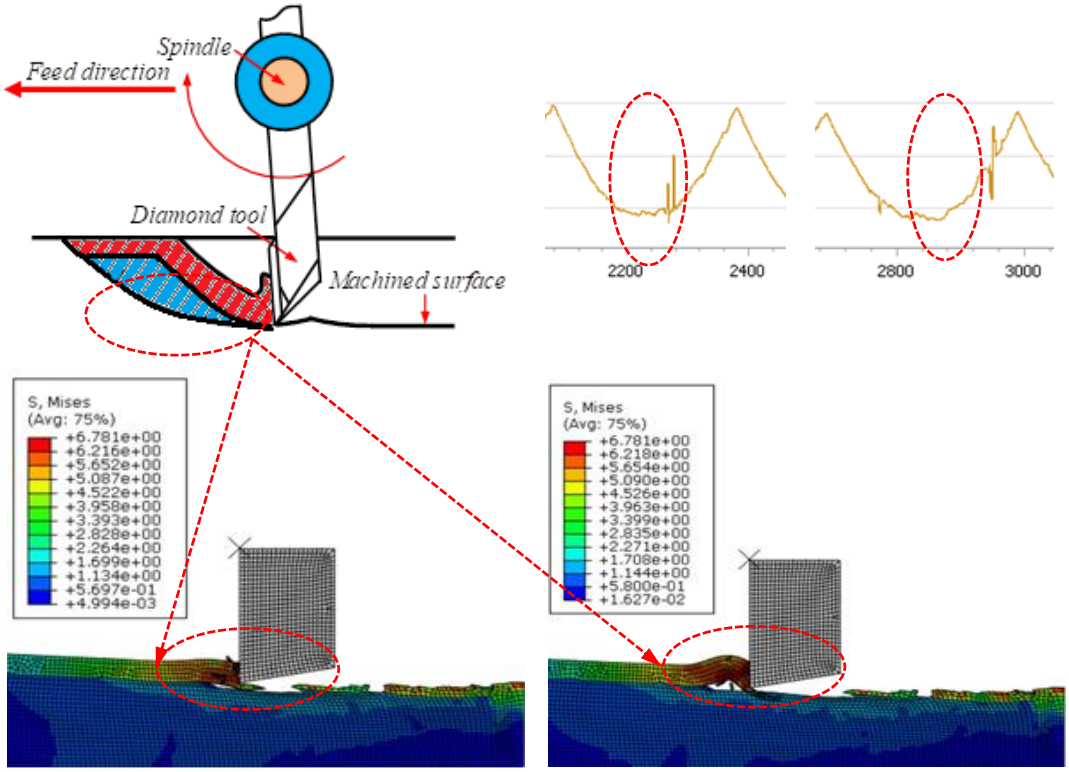

Fig.13 Tool-in causes void formation of inner layer in 2D FE simulation of UPFC

With the continuous of cutting, the cutting chip will be fully formed. Fig.14 shows the comparison of simulated cutting chip formation and the inspected cutting chip morphology, it is obvious that the morphology of cutting chip is consistent with the simulation one, which indicates that the simulation result is reliable.

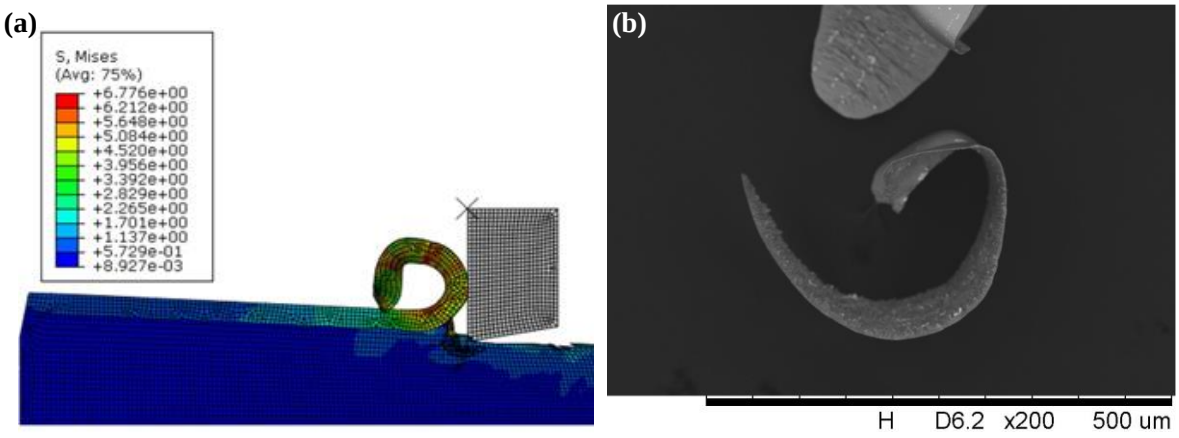

Fig.14 Comparison of chip morphology between simulated result and measured one

Fig.15 has demonstrated the process of SRP formation. When the diamond tool enters the workpiece surface, both the surface layer and inner layer grain will receive the same

cutting force provided by the diamond tool. The surface layer next to diamond tool is deformed and damaged because of shear stress. As the fracture strain of surface layer and inner layer approximate to 1.16 according to calculation, the inner layer will damage first as it will only take about 0.3Mpa for inner layer reach fracture strain while the surface layer is still in its elastic stage. Micro voids will be formed in the inner grain layer when the diamond tool cuts the surface layer, which is marked with yellow circle as shown in Fig.15 (a). When the diamond tool finishes the yellow circle area cutting and passes over, some of the marks will be left and therefore causes SRP formation, as is shown in Fig.15 (c).

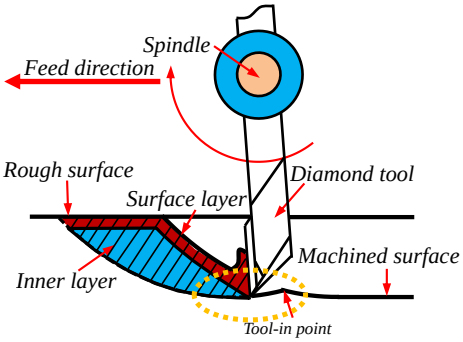

(a) Tool-in. Yellow circle area already forms voids before tooling arrives.

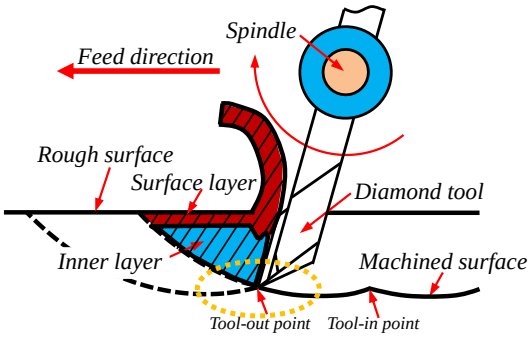

(b) Tool-out. Tooling cut inside the yellow circle area, voids cause rough surface.

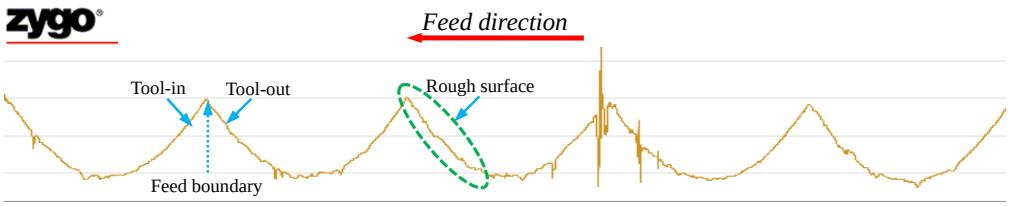

(c) Surface profile. Rough surface at tool-out side

Fig.15 Cutting chip and SRP generation in a fly cutting process

The formation of SRP at the tool-out area of a tool feed imprint certainly affects the machined surface roughness and even its function. One effective method to suppress the occurrence of SRP is to reduce the chip thickness, which will reduce the area affected by cutting force. With the reduction of chip thickness, the number surface layer grain changes little but the number of inner layer grain will be much less, therefore the voids formation area will decrease. From the cutting kinematics of UPFC, reducing the feed per revolution (mm/rev) will decrease the chip thickness and thus reduce the area affected by cutting force.

The feed per revolution can be calculated by:

$$f' = \frac{f}{s_p} \tag{9}$$

Where f' is the feed per revolution, f is the feed rate in the unit of mm/min, s_p is the spindle speed in the unit of rev/min. From Eq.(9), increase the spindle speed or decrease the feed rate can reduce the feed per revolution.

Fig.16 shows the surface topography of UPFC under the spindle speed of 500,1500,3000,4500 rpm respectively. It is found that the spindle speed clearly affects the machined surface topography, at the spindle speeds of 500 rpm, the feed boundary is quite clear, and SRPs are found on the tool-out area, in contrast, a smooth surface is formed at the tool-in area. The distribution of SRPs is reducing with the increase of spindle speed, notably, at the spindle speed of 4500rpm, the feed boundary is hard to be distinguished and SRPs cannot be found yet.

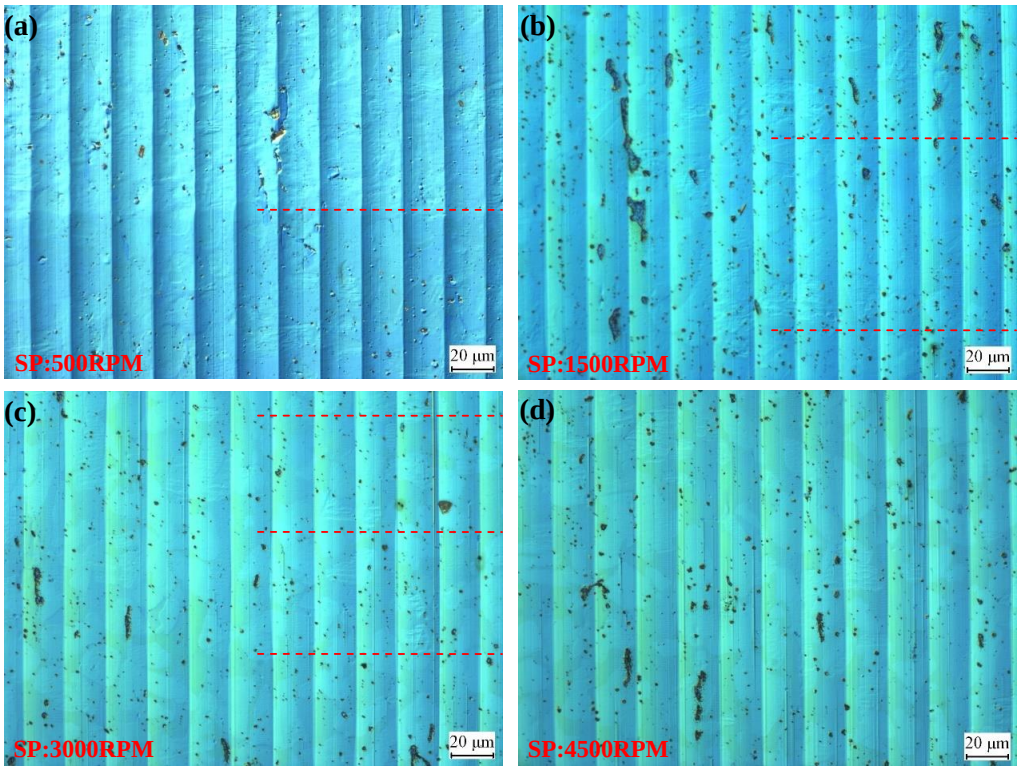

Fig.16 Surface topography of UPFC under different spindle speed (measured by Olympus

BX60 optical microscope)

Similar phenomena can also be found at different feed rate, as is shown in Fig.17, SRPs at tool-out area are easy to be identified at the feed rate of 900mm/min; while with the decrease of feed rate, the length of tool feed imprint in a rotary cutting become shorter, the SRPs are hard to be identified too.

However, cutting depth was found has no significant influence on the SRP formation, because under other cutting parameters are fixed, changing cutting depth only change the chip length, it has little effect on reducing chip thickness.

This group of experimental results confirmed that increase of spindle speed and reducing feed rate can suppress the SRP formation and improve the surface finish. However, cutting depth has little influence on the SRP formation.

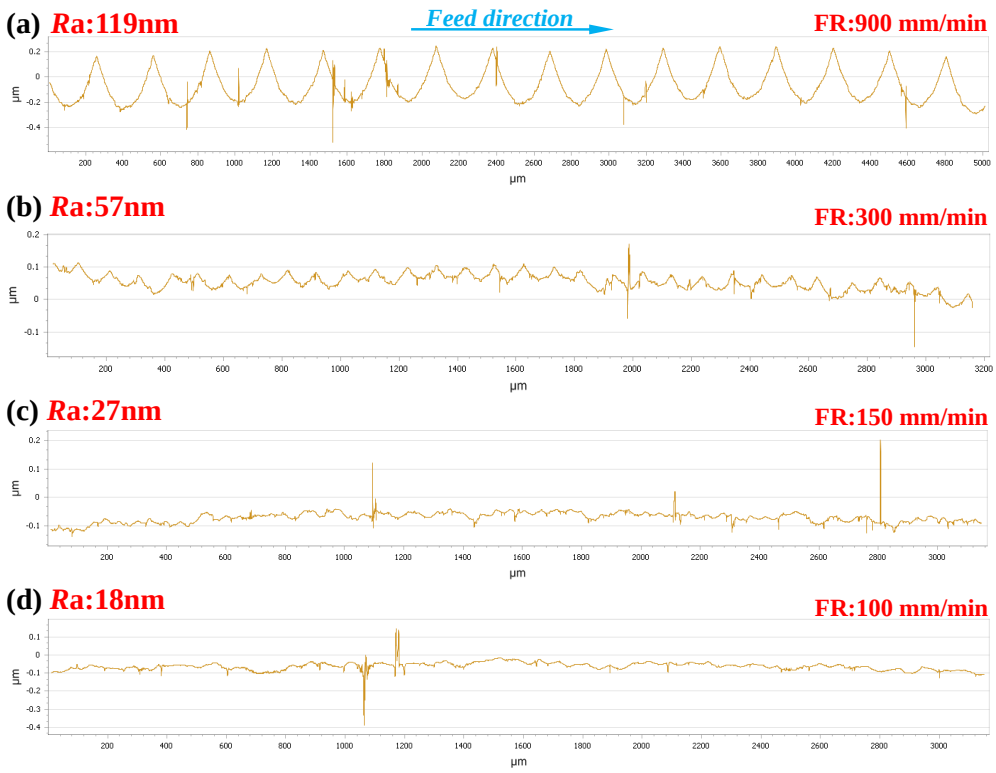

Fig.17 Sectional profile of tool feed imprint in a white light interferometer measurement at difference feed rate (Zygo Nexview)

6. Conclusions

In this research, the origin of SRP and its affecting factors is investigated, and the influence of size effect in UPFC on the formation of SRP is explored. A hybrid constitutive Johnson Cook model is established and whereby a finite element (FE) simulation was conducted to analyze the generation of the SRPs. Some specific conclusions drawn from the research are:

1. Cutting experiments showed an interesting phenomenon: surface quality was poor on the tool-out area of each tool feed imprint, however was smooth on tool-in area. Poor surface is caused by the SRP formation on the tool-out area, the SRP has irregular shape and distribution.

2. A hybrid constitutive Johnson Cook model considering the surface layer effect was established. The model shows that the strain energy difference of surface layer grain and inner layer grain is the main reason causes SRP formation.

3. A two-dimension FE simulation of the UPFC process was conducted in the Abaqus® FEA software, the FE simulation result shows that micro voids formulated in the inner layer when diamond tooling cuts the surface layer, which thus causes SRP formation.

4. In order to eliminate the SRP to obtain good surface roughness, the influence of cutting parameters is investigated and revealed. It is found that reduction of feed rate and increase of spindle speed will suppress the occurrence of SRP, while cutting depth has no obvious effect on the SRP generation. Changing these two cutting parameters makes the cutting tool cut through the surface layer without contacting inner layer of the specimen, which thus improves the surface ending of the specimen.

The present research provides a good understanding of the generation of SRP at tool-out due to size effect and cutting mechanism of UPFC, which could be used to suppress the occurrence of SRP of UPFC and thus improve machined surface finish.

Acknowledgements

The work described in this paper was supported by the grants from the National Natural Science Foundation of China (Grant No. 51505297, 51705333), the Natural Science Foundation of Guangdong Province (Grant No. 2017A030313295, 2017A030310352), the Shenzhen Science and Technology Program (Grant No. JCYJ20160422170026058, JCYJ20160520175255386), and the Shenzhen Peacock Technology Innovation Project (Grant No. KQJSCX20170727101318462).

References

[1]. Zhang G, To S, Xiao G. A novel spindle inclination error identification and compensation method in ultra-precision raster milling. International Journal of Machine Tools & Manufacture 2014; 78(3):8-17.

[2]. Wu Y, Peng W, Liu Y. A novel fabrication method for micro optical waveguide mold based on fly-cutting technology. Optik - International Journal for Light and Electron Optics 2013; 124(9):867-869.

[3]. Zhu Z, To S, Zhang S. Theoretical and experimental investigation on the novel end-fly-cutting-servo diamond machining of hierarchical micro-nanostructures. International Journal of Machine Tools & Manufacture 2015; 94:15-25.

[4]. Zhu Y H, To S, Lee W B, et al. Ultra-precision raster milling-induced phase decomposition and plastic deformation at the surface of a Zn–Al-based alloy. Scripta Materialia 2010; 62(2):101-104.

[5]. Zhang S J, To S. Deformation-induced phase changes of Zn-Al alloy during ultra-precision raster milling. International Journal of Advanced Manufacturing Technology 2016; 88(5-8):1-7.

[6]. Wang S, To S, Chan C Y, et al. A study of the cutting-induced heating effect on the machined surface in ultra-precision raster milling of 6061 Al alloy. International Journal of Advanced Manufacturing Technology 2010; 51(1-4):69-78.

[7]. Zhang G, To S, Zhang S, et al. Case study of surface micro-waves in Ultra-precision Fly Cutting. Precision Engineering 2016; 46:393-398.

[8]. Zhang G, To S, Xiao G. The relation between chip morphology and tool wear in ultra-precision raster milling. International Journal of Machine Tools & Manufacture 2014; 80-81(4):11-17.

[9]. Zhang G, To S, Xiao G. Novel tool wear monitoring method in ultra-precision raster milling using cutting chips. Precision Engineering 2014; 38(3):555-560.

[10]. Zhang G, To S. A novel online surface quality evaluation method in ultra-precision raster milling using cutting chips. Journal of Materials Processing Technology 2014; 219:328-338.

[11]. Zhang G, To S, Zhang S. Evaluation for tool flank wear and its influences on surface roughness in Ultra-precision Fly Cutting. International Journal of Mechanical Sciences 2016; 118:125-134.

[12]. Wang S J, To S, Chen X, et al. An integrated optimization of cutting parameters and tool path generation in ultraprecision raster milling. International Journal of Advanced Manufacturing Technology 2014; 75(9-12):1711-1721.

[13]. Lee W B, Cheung C F. A dynamic surface topography model for the prediction of nano-surface generation in ultra-precision machining. International Journal of Mechanical Sciences 2001; 43(4):961-991.

[14]. Cheung CF, Lee WB, To S. A framework of a model-based simulation system for predicting surface generation in ultra-precision raster milling of freeform surfaces, Annual of American Society for Precision Engineering Proceedings, Orlando, Florida, (2004):1149-1156.

[15]. Cheung C F, Kong L B, Lee W B, et al. Modelling and simulation of freeform surface generation in ultra-precision raster milling. Proceedings of the Institution of

Mechanical Engineers Part B Journal of Engineering Manufacture 2006; 220(11):1787-1801.

[16]. Cheng M N, Cheung C F, Lee W B, et al. Theoretical and experimental analysis of nano-surface generation in ultra-precision raster milling. International Journal of Machine Tools & Manufacture 2008; 48(10):1090-1102.

[17]. Kong L B, Cheung C F, To S, et al. An investigation into surface generation in ultra-precision raster milling. Journal of Materials Processing Technology 2009; 209(8):4178-4185.

[18]. Kong L B, Cheung C F. Prediction of surface generation in ultra-precision raster milling of optical freeform surfaces using an Integrated Kinematics Error Model. Advances in Engineering Software 2012; 45(1):124-136.

[19]. Wang S J, To S, Cheung C F. An investigation into material-induced surface roughness in ultra-precision milling. International Journal of Advanced Manufacturing Technology 2013; 68(1-4):607-616.

[20]. Zhang S J, To S. A theoretical and experimental study of surface generation under spindle vibration in ultra-precision raster milling. International Journal of Machine Tools & Manufacture 2013; 75(12):36-45.

[21]. Zhang S J, To S, Zhang S J. The effects of spindle vibration on surface generation in ultra-precision raster milling. International Journal of Machine Tools & Manufacture 2013; 71(2):52-56.

[22]. An C H, Zhang Y, Xu Q, et al. Modeling of dynamic characteristic of the aerostatic bearing spindle in an ultra-precision fly cutting machine. International Journal of Machine Tools & Manufacture 2010; 50(4):374-385.

[23]. Wang JL, Fu MW, Shi SQ, Korsunsky AM. Size effect and plastic strain gradient on the springback behavior of metallic materials in microbending process. International

Journal of Mechanical Sciences 2018; https://doi.org/10.1016/j.ijmecsci.2018.07.027.

[24]. J. H. Deng, M. W. Fu, W. L. Chan, Size effect on material surface deformation behavior in micro-forming process, Materials Science and Engineering: A, Volume 528, Issues 13–14, 25 May 2011, Pages 4799-4806

[25]. Prasitthipayong A, Vachhani S J, Tumey S J, et al. Indentation size effect in unirradiated and ion-irradiated 800H steel at high temperatures. Acta Materialia 2018; 144:896-904.

[26]. Chan W L, Fu M W, Yang B. Study of size effect in micro-extrusion process of pure copper. Materials & Design 2011; 32(7):3772-3782.

[27]. Bissacco G, Hansen H N, Chiffre L D. Size Effects on Surface Generation in Micro Milling of Hardened Tool Steel. CIRP Annals - Manufacturing Technology 2006; 55(1):593-596.

[28]. Lai X, Peng L, Hu P, et al. Material behavior modelling in micro/meso-scale forming process with considering size/scale effects. Computational Materials Science 2008; 43(4):1003-1009.

[29]. Peng L, Hu P, Lai X, et al. Investigation of micro/meso sheet soft punch stamping process – simulation and experiments. Materials & Design 2009; 30(3):783-790.

[30]. M. Wang, D. Wang, T. Kups, P. Schaaf, Size effect on mechanical behavior of Al/Si3N4 multilayers by nanoindentation, Materials Science and Engineering: A, Volume 644, 17 September 2015, Pages 275-283.

[31]. Shun-Peng Zhu, Stefano Foletti, Stefano Beretta, Evaluation of size effect on strain-controlled fatigue behavior of a quench and tempered rotor steel: Experimental and numerical study, Materials Science and Engineering: A, Volume 735, 26 September 2018, Pages 423-435.

[32]. Martin Leitner, Christian Garb, Heikki Remes, Michael Stoschka, Microporosity and

statistical size effect on the fatigue strength of cast aluminium alloys, Materials Science and Engineering: A, Volume 707, 7 November 2017, Pages 567-575.

[33]. Peng L F, Mao M Y, Fu M W, et al. Effect of grain size on the adhesive and ploughing friction behaviours of polycrystalline metals in forming process. International Journal of Mechanical Sciences 2016; 117:197-209.

[34]. Fu M W, Wang J L, Korsunsky A M. A review of geometrical and microstructural size effects in micro-scale deformation processing of metallic alloy components. International Journal of Machine Tools & Manufacture 2016; 109:94-125.

[35]. Kim Y C, Gwak E J, Ahn S M, et al. Indentation size effect for spherical nanoindentation on nanoporous gold. Scripta Materialia 2018; 143:10-14.

[36]. Kim K W, Lee W Y, Sin H-C. A finite element analysis for the characteristics of temperature and stress in micro-machining considering the size effect. International Journal of Machine Tools & Manufacture 1999; 39(9):1507-1524.

[37]. Shaw M C. The size effect in metal cutting. Sadhana 2003; 28(5):875-896.

[38]. Dinesh D, Swaminathan S, Chandrasekar S, Farris TN. An intrinsic size-effect in machining due to the strain gradient. Proc. ASME-Int. Mech .Eng. Conf. 2001;1–8.

[39]. Chen N, Chen M, Wu C, et al. Research in minimum undeformed chip thickness and size effect in micro end-milling of potassium dihydrogen phosphate crystal. International Journal of Mechanical Sciences 2017; 134:387-398.

[40]. Weng J, Zhuang K, Zhu D, et al. An analytical model for the prediction of force distribution of round insert considering edge effect and size effect. International Journal of Mechanical Sciences 2018; 138–139: 86-98.

[41]. Liu K, Melkote S N. Finite element analysis of the influence of tool edge radius on size effect in orthogonal micro-cutting process. International Journal of Mechanical Sciences 2007; 49(5):650-660.

[42]. Oliveira F B D, Rodrigues A R, Coelho R T, et al. Size effect and minimum chip thickness in micromilling. International Journal of Machine Tools & Manufacture 2015; 89:39-54.

[43]. Johnson G R, Cook W H. A. Constitutive model and data for metals subjected to large strains, high strain rates and high temperatures. In: Proceedings of the 7th International Symposium on Ballistics. Den Haag, The Netherlands 1983;541–543.

[44]. Ran J Q, Fu M W. A hybrid model for analysis of ductile fracture in micro-scaled plastic deformation of multiphase alloys. International Journal of Plasticity 2014; 61(10):1-16.

[45]. Petch N J. The Cleavage Strength of Polycrystals. J Iron Steel Inst 1953; 174(1):25--28.

[46]. Hansen N. Polycrystalline strengthening. Metallurgical Transactions A 1985; 16(12):2167-2190.

[47]. Argon AS. Strengthening Mechanisms in Crystal Plasticity. Oxford University Press. 2008.

[48]. Armstrong R, Codd I, Douthwaite R M, et al. The plastic deformation of polycrystalline aggregates. Philosophical Magazine 1962; 7(73):45-58.

[49]. Armstrong RW, The yield and flow stress dependence on polycrystal grain size. In: Baker, T.N., Petch, Norman J. (Eds.), Yield, Flow and Fracture Polycrystals, 1982; 1–31.

[50]. RodríGuez R, Gutierrez I. Correlation between nanoindentation and tensile properties : Influence of the indentation size effect. Materials Science & Engineering A 2003; 361(1–2):377-384.

[51]. Hillerborg A, Modéer M, Petersson P E. Analysis of crack formation and crack growth in concrete by means of fracture mechanics and finite elements. Cement & Concrete Research 1976; 6(6):773-781.